Influence of flow properties on a structure of a mineral wool primary layer

Tom Bajcar *, Bogdan Blagojević, Brane Širok, Matevž Dular

Faculty of Mechanical Engineering, University of Ljubljana, Aškerčeva 6, SI – 1000 Ljubljana, Slovenia

Abstract

Mineral wool primary layer formation is influenced by the aerodynamic characteristics of the blow-away airflow and the secondary surrounding airflow. The distribution of mineral wool fibres in the primary layer was determined experimentally using a computer-aided visualization method. The flow properties in the region where the primary layer is formed were analysed. Numerical simulations with experiment-based boundary conditions were performed. The numerically obtained profile of mineral wool thickness at the collection chamber outlet agreed with the results of the experiment. Presented numerical model confirms that the forming of the primary layer is significantly dependent on local aerodynamic characteristic of the airflow in the collection chamber. Interaction between the local anomalies on the forming layer and the corresponding aerodynamic effects in the surrounding region was also analysed.
© 2007 Elsevier Inc. All rights reserved.

1. Introduction

Mineral wool is a general name for various inorganic insulation materials made of fibres. Mineral wool is usually divided into different subgroups depending on the raw materials they are made of, e.g. rock wool, glass wool and slag wool.

The most frequently used raw materials for mineral wool production are diabase, dolomite, granite, basalt, limestone, etc. Because of its amorphous structure, mineral wool has excellent sound and thermal insulation properties. There are several production methods for mineral wool fibres, with a wide variation of quality and quantity of the final product [1]. The most commonly used mineral wool production process is the fiberisation process of molten rock on fast rotating spinning discs [2–4]. At the furnace outlet, the melt should be homogeneous, single-phased, without any solid inclusions, and can be character-

ised by density, surface tension and viscosity. During the mineral wool formation process, the fibres are usually formed on a four-disc spinning machine. During fibre formation, the moistening process of fibres with phenol solution also takes place. The formed fibres enter a blow-away airflow, which blows around the circumference of the spinning discs and flows in the axial direction of the discs towards the perforated mesh. This airflow transports mineral wool fibres into a collection chamber where the fibres settle onto a moving perforated mesh. Mineral wool fibres have a diameter of about 5 μm and length of about 10 mm. Beside the basic blow-away airflow that transports fibres to the region of the moving perforated mesh, a secondary airflow is formed in the front part of the collection chamber and consists of the surrounding air that enters the collection chamber because of the suction; both the blow-away and the secondary airflows are sucked out of the chamber through a suction duct at the back of the chamber. This suction (i.e. the suction airflow) ensures negative pressure in the collection chamber, and directs the blow-away airflow (and thus the mineral wool fibres) onto the perforated

Nomenclature

A	average grey level intensity; dimensionless	x	lateral coordinate; m
E	grey level intensity of a pixel; dimensionless	y	longitudinal coordinate; m
K	successive window number; dimensionless		
k	turbulent kinetic energy; $m^2\,s^{-2}$	*Greek symbols*	
p	pressure; Pa	α	inverse effective turbulent Prandtl number; dimensionless
S_M	momentum source; $kg\,m^{-2}\,s^{-2}$		
T	time; s	ε	turbulent kinetic energy dissipation rate; ms^{-3}
t	number of a successive image in a sequence; dimensionless	μ	viscosity; $kg\,m^{-1}\,s^{-1}$
		ρ	density; $kg\,m^{-3}$
v	velocity; ms^{-1}	$\sigma(v)$	local velocity standard deviation; ms^{-1}

mesh. The volume flow ratio of the blow-away airflow to the suction airflow from the collection chamber ranges from 1:10 to 1:12 [5]. Fig. 1 schematically presents the collection chamber.

The primary layer forms between points A and B (Fig. 1). Beyond the point B in the direction of the perforated mesh movement, the primary layer is fully formed. The settlement of mineral wool fibres onto the perforated mesh and the formation of the primary layer depend on the airflow direction onto the perforated mesh. Primary layer formation is also influenced by the structure of the perforated mesh and its movement towards the outlet aper-

ture at the top of the collection chamber, where the primary layer is ultimately formed. Using experimental research, it was established [5,6] that the kinematics of the blow-away airflow and of the secondary airflow has the main influence on primary layer formation. In both works the relations between the integral parameters of mineral wool production and mineral wool distribution were researched. It was established that the uniform mineral wool distribution in the primary layer significantly affects the final product quality. The primary layer quality depends mainly on the airflow properties in the region where primary layer is formed. Fig. 2a shows a suitably
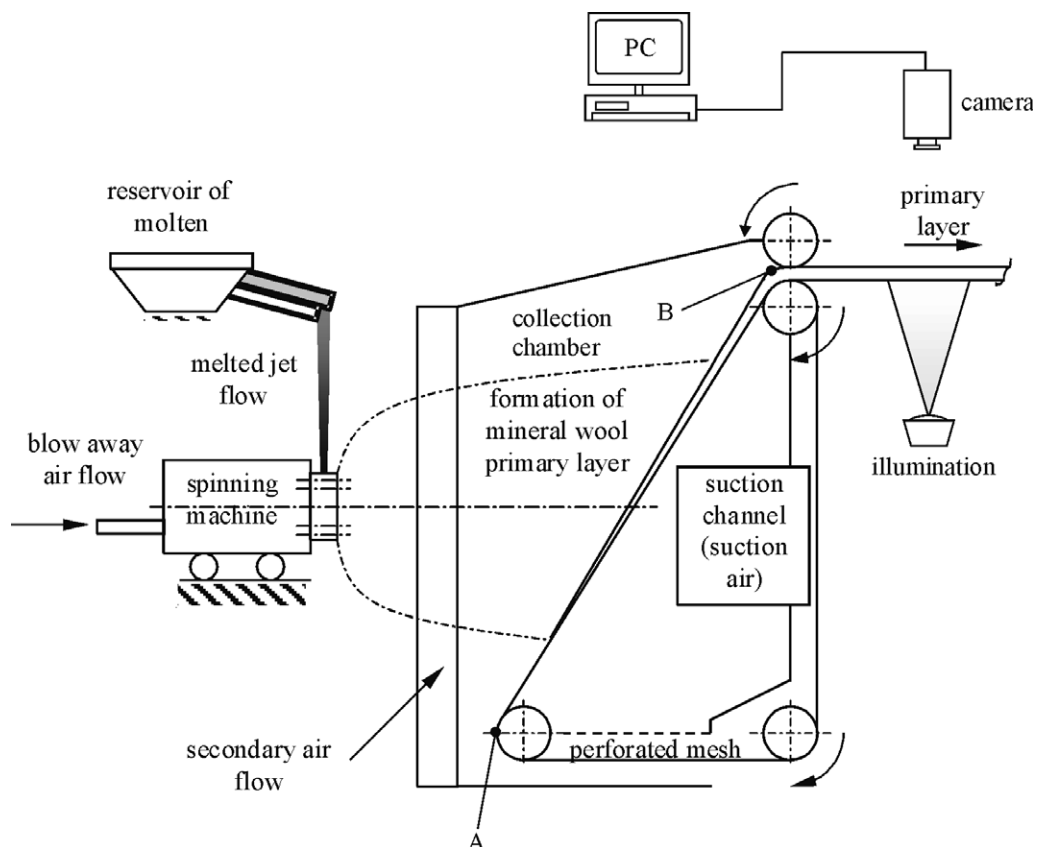

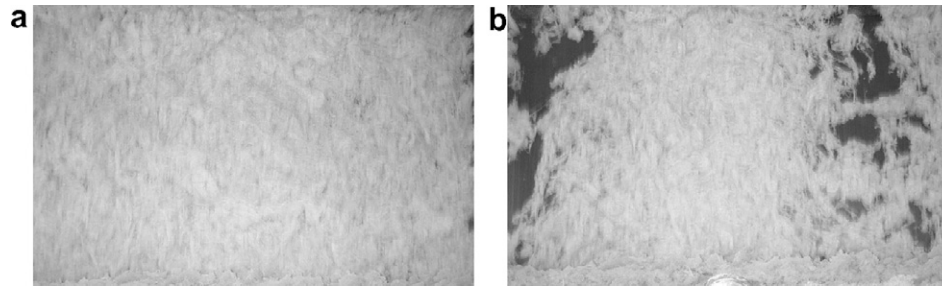Fig. 1. Schematic view of a collection chamber.

Fig. 2. Structure of a primary layer, (a) homogeneous; (b) non-homogeneous.

formed primary layer, and Fig. 2b an unsuitably formed primary layer [7].

In the case of a non-uniform primary layer (Fig. 2b) the local tearing of primary layer occurs as the result of local velocity extremes, velocity field asymmetry, and pulsation of airflow. It was also established that the uniformity and continuity of a formatted primary layer are dependent on the axial symmetrical uniform velocity field in the region where the air flows through the primary layer and the perforated mesh. This paper concentrates on the kinematics analysis of the airflow in the collection chamber and on the analysis of the influence of the airflow on the forming of the primary layer. Due to difficulties in acquiring experimental results of actual flow conditions in an operating collection chamber, the presented analyses are mostly based on numerical simulations and on experimentally acquired boundary conditions.

The geometry of the collection chamber as well as certain boundary condition values result from the measurements performed on an existing collection chamber. The measurement results include data on blow-away airflow [5] and mineral wool distribution in the region of the perforated mesh in the collection chamber and at the wool outlet at the top of the chamber [7].

2. Visualization method for measurement of primary layer homogeneity

A method of computer-aided visualization was used for quantitative description of the uniformity of mineral wool primary layer [5]. The method is based on the acquisition of subsequent images of mineral wool primary layer immediately after its exit from a collection chamber (Fig. 1). The targeted structure of the mineral wool primary layer should be uniform and isotropic on a local scale, and without surface interruptions on a larger scale. The primary wool layer should also be as thin as possible for low-density products. This is consistent with the optically uniform isotropic structure of intertwined mineral wool samples.

2.1. Cumulative structure of primary layer

The cumulative structure of primary layer at the wool outlet on the top of the collection chamber (i.e. at point

B in Fig. 1) can be measured using computer-aided visualization, spatially and over time. Images were acquired using a Sony Hi8 TR820E camera with a resolution of 480×640 pixels at a frame rate of 25/s. The images were digitised using the Ulead Video Studio 5 DV software package and analysed using the Dynascan software [2]. Illumination was carried out by means of a neon-tube lamp, which was placed underneath the perforated mesh (Fig. 1) along its entire width in such a way that the generated light penetrated the perforated mesh and primary layer on the upper surface of the mesh (Fig. 3). The perforated mesh obstructed the penetrating light to some extent, but this obstruction remained unchanged during the whole experiment. Apart from that, the camera was posed directly opposite the illumination source, its axis being perpendicular to the direction of the perforate mesh movement. In this way, the influence of eventual shadows cast by the perforated mesh on the primary layer were minimised.

The analysis was performed in every image in a sequence of selected windows, arranged as shown in Fig. 3. The width and the height of each window were set to 5 and 14 pixels, respectively. The height of the window thus corresponded to the vertical movement of the primary layer in the time period between two images (Fig. 3). One hundred and twenty five windows were selected in each image to cover the whole width (2.573 m ≡ 625 pix) of the perforated mesh. The windows were always at the same fixed position on each image; the only moving object was the
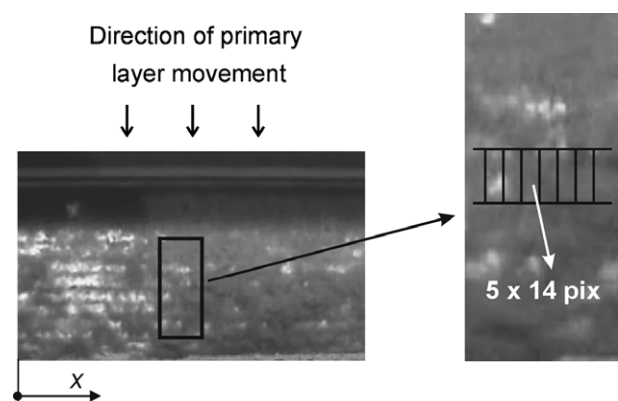

Fig. 3. Arrangement of windows for analysis on each image.

perforated mesh with the primary layer, which moved in the vertical direction from one image to another. For every image in the sequence, the average intensity $A(K, t)$ was calculated for each window [5]:

$$A(K, t) = \sum_l \sum_m E(l, m). \tag{1}$$

Here, K denotes the successive window number in each frame, and t denotes the successive acquired image. The transverse position of window k is defined with the proportional expression $x = 0.0206 \cdot K - 0.0103$, where x denotes the horizontal coordinate (Fig. 3). The intensity $E(l, m)$ of each pixel ranges from 0 to 255, corresponding to an 8-bit resolution of the camera. l and m are the coordinates of the pixels inside the window (K, t). In the particular window the variable $A(K, t)$ denotes the momentary present portion of mineral wool. In the case of a thin primary layer a hypothesis describing proportional dependence between variable $A(K, t)$ and the local structure (e.g. local mass ρ) of primary layer can be set:

$$\rho(x, t) \propto A(x, t). \tag{2}$$

The distribution of mineral wool perpendicular to the primary layer movement is estimated using the time averaged local mass of primary layer $\rho(x, t)$:

$$\overline{\rho(x)} = \frac{1}{T} \int_0^T \rho(x, t) \mathrm{d}t. \tag{3}$$

Using Eq. (3) the mineral wool distribution in the final product is determined. The mineral wool distribution for the observed process of mineral wool production is shown in Fig. 4.

Fig. 4 shows an asymmetrical and saddle-shaped distribution of mineral wool, which deviates from the uniform distribution that assures homogeneous mechanical and thermal isolation properties in a final product. This asymmetry is the result of combined flows of the blow-away airflow and secondary airflow, as well as of the mineral fibre transport on the moving perforated mesh. Apart from the non-homogeneous mineral wool distribution in the primary layer, a local increase in standard deviation can also be observed in Fig. 4, which relates to increased fluctua-

tions of the primary layer thickness. The latter is increased in regions of increased standard deviation and this phenomenon can be related to the blow-away airflow field as well. The measured distribution of mineral wool can be treated as a cumulative result of the settlement of mineral wool fibres in the whole active region of the collection chamber and it represents the key information about primary layer quality. The settlement of mineral wool fibres inside the collection chamber is expected to be strongly influenced by the velocity field of the airflow. The interconnection between the primary layer structure (local mass) and the airflow velocity field will be the main topic through the rest of the paper.

2.2. Local distribution and Fourier analysis of the primary layer structure

In order to investigate the dependence of primary layer structure on the airflow velocity field inside the collection chamber, a distribution of primary layer structure at selected longitudinal regions on the perforated mesh was studied. For this purpose, a narrow window of 1 (length) × 14 (height) pixels was placed over images of mineral wool primary layer at different positions x using Dynascan software. In this case, the intensity of individual pixels E was recorded for each pixel in the window individually rather than calculating average value of intensity A for the whole window. Thus, from each image 14 different values of E (one for each pixel in the window) could be obtained. Since the whole sequence amounted 250 images, there were $14 \cdot 250 = 3500$ values of E gathered for the primary layer structure assessment on the selected position x of the perforated mesh. When sorted in time successive order, it was possible to calculate a power spectrum from the values of E at selected positions x using the Fast Fourier Transformation. Figs. 5–7 represent histograms of primary layer structure distribution at different positions x on the perforated mesh.

It is of interest that the values of E (Figs. 5a, 6a and 7a) show a skewed distribution, the peak value being moved slightly to the left in each case. Figs. 5b, 6b and 7b show power spectrum of the values of E at the selected positions x. There is also a dashed straight line that represents Kolmogorov's "cascade $-5/3$ law" for turbulence decay [8]. It can be seen from Figs. 5b, 6b and 7b that the slope of the power spectrum matches quite well with the slope of the dashed line that represents the $-5/3$ law. This might be another sign that the turbulent velocity field inside the collection chamber could significantly influence the structure of the primary layer. Nevertheless, some further experimental work should eventually be carried out to thoroughly confirm this conclusion.

2.3. Visualisation of primary layer in the collection chamber

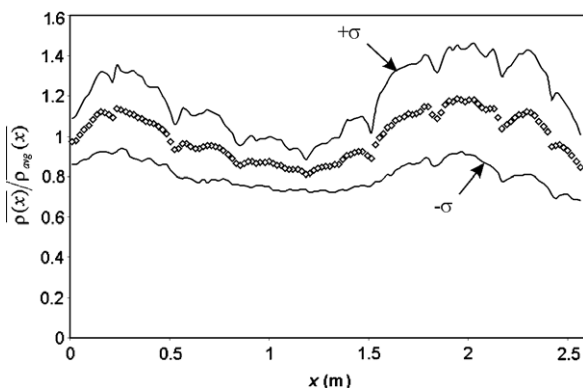The next step was to get a sequence of instant images of the whole length of the perforated mesh inside the col-
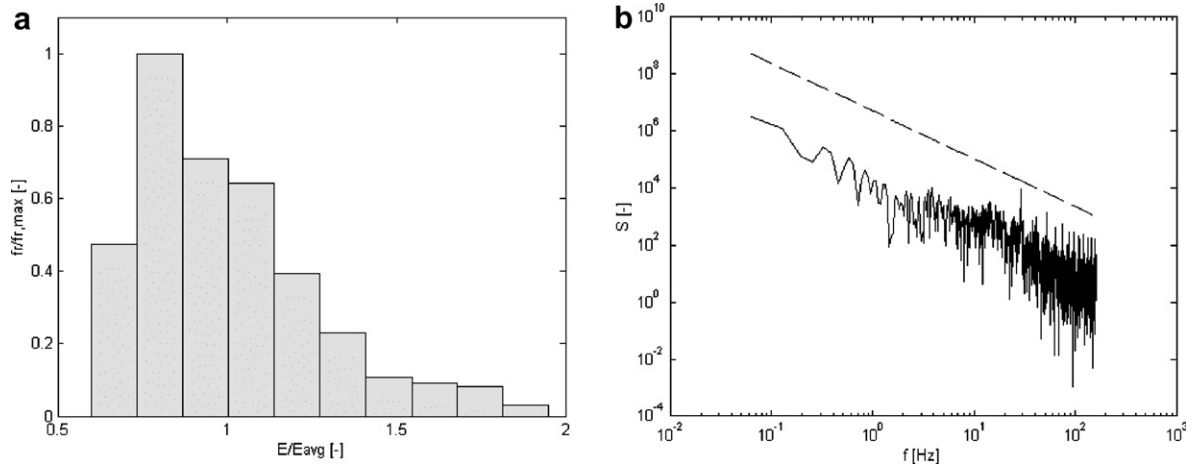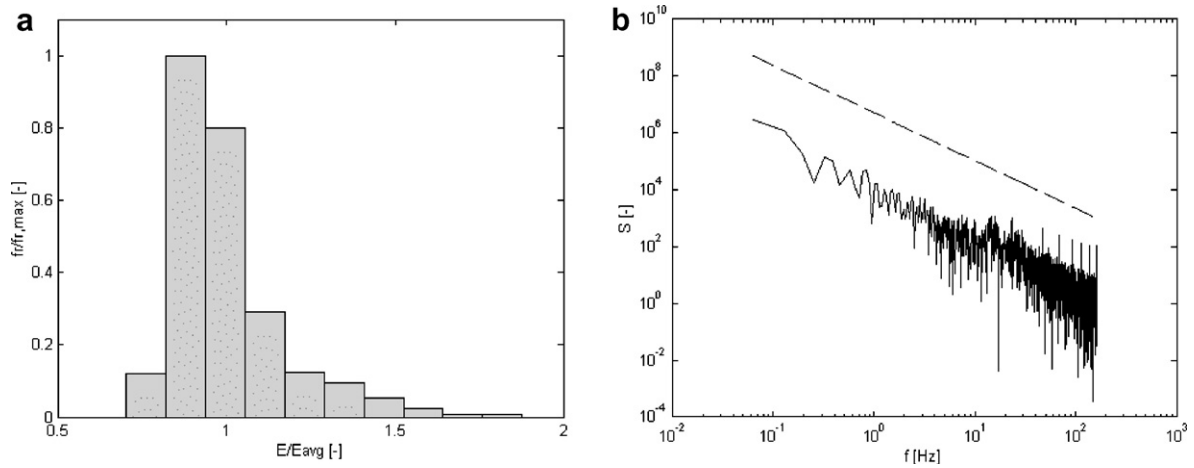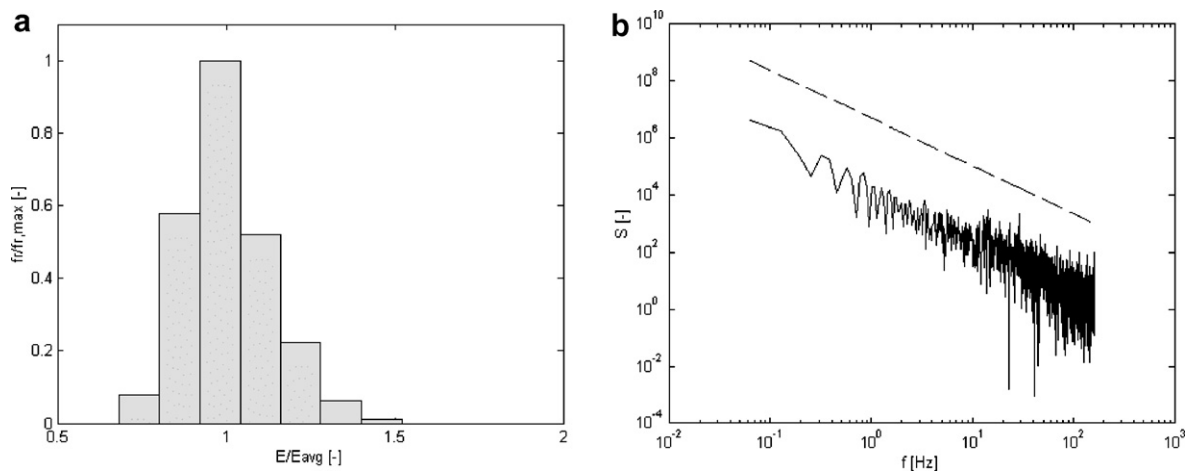

Fig. 4. Mineral wool distribution estimated using variable $\overline{\rho(x)}$.

Fig. 5. Distribution (a) and power spectrum (b) of values E at $x = 53.5$ mm.

Fig. 6. Distribution (a) and power spectrum (b) of values E at $x = 1286.5$ mm.

Fig. 7. Distribution (a) and power spectrum (b) of values E at $x = 2519.5$ mm.

lection chamber. The length of the perforated mesh between points A and B (Fig. 1) was 7 m, which corresponded to 1700 pixels. Since the images inside the collection chamber could not be acquired, the images taken at the wool outlet on the top of the collection chamber were used to gain information about the structure of primary layer inside the collection chamber. For this purpose, the same method was used as in Section 2.1, except that

now there were only 25 windows placed in a single row over each image. Dimensions of each window were 25 pixels (width) × 14 pixels (height), so the row of windows covered the whole width (=625 pixels) of the perforated mesh. With the selected height of the windows, 121 consecutive images were needed for each window to cover the whole length of the perforated mesh (=1700 pixels). For every image in the sequence, the average intensity $A(K,t)$ (Eq. (1)) was calculated for each window in the same manner as in Section 2.1. To get an instant picture of the primary layer on the whole perforated mesh between points A and B at a particular moment in time, a linear law was applied to simulate the change in local mass ρ of the primary layer on the perforated mesh in the longitudinal direction from point A to point B (Fig. 1). For this purpose, the values of $A(K,t)$ of successive images $t = 1, 2, 3, \ldots, 121$ were multiplied by a factor $1 - (t-1)/120$. Thus, the values of $A(K,1)$ remained unchanged, while all other values of $A(K,t)$ decreased linearly with the increasing t until they reached value 0 at the 121st image. The whole matrix of values of A then represented the primary layer on the perforated mesh inside the collection chamber between points A and B at the time, when the image with index $t = 1$ reached the point B.

By changing the index t of the first image and applying analogous procedure as described above, it was possible to extract images of the primary layer on the perforated mesh at different moments in time. Fig. 8 shows successive images of the primary layer structure inside the collection chamber. The time shift between two neighbouring images is 0.4 s.

Brighter areas in Fig. 8 represent the regions on the perforated mesh with thicker primary layer. Bottom of each image in Fig. 8 depicts the perforated mesh at point A, i.e. at the bottom of the collection chamber, where there are no wool fibres attached to the perforated mesh.

Images of the primary layer structure inside the collection chamber were compared to the velocity field above the perforated mesh. Velocity field inside the collection chamber was calculated using the methods of numerical analysis.

3. Numerical analysis

Numerical simulations with experiment-based boundary conditions were performed. The goal of the numerical study was to investigate the hypothesis that the forming of the primary layer is significantly dependent on local aerodynamic characteristic of the airflow in the collection chamber. Interaction between the local anomalies on the forming layer and the corresponding aerodynamic effects in the surrounding region was also analysed.

CFD code Fluent 6.1.22 was used to calculate the flow inside the chamber. It is a three-dimensional structured mesh code that solves a set of Reynolds-averaged Navier–Stokes equations (RANS). The numerical model uses an implicit finite volume scheme, based on a SIMPLE algorithm [9,10]. A second-order upwind differentiating scheme was used.

In the RANS approach the mass (Eq. (4)) and the momentum (Eq. (5)) conservation equations together with the equations of the turbulence model (Eqs. (6) and (7)) form a closed set of equations.

The mass conservation equation reads

$$\frac{\partial \rho}{\partial t} + \frac{\partial(\rho \bar{v}_j)}{x_j} = 0. \tag{4}$$
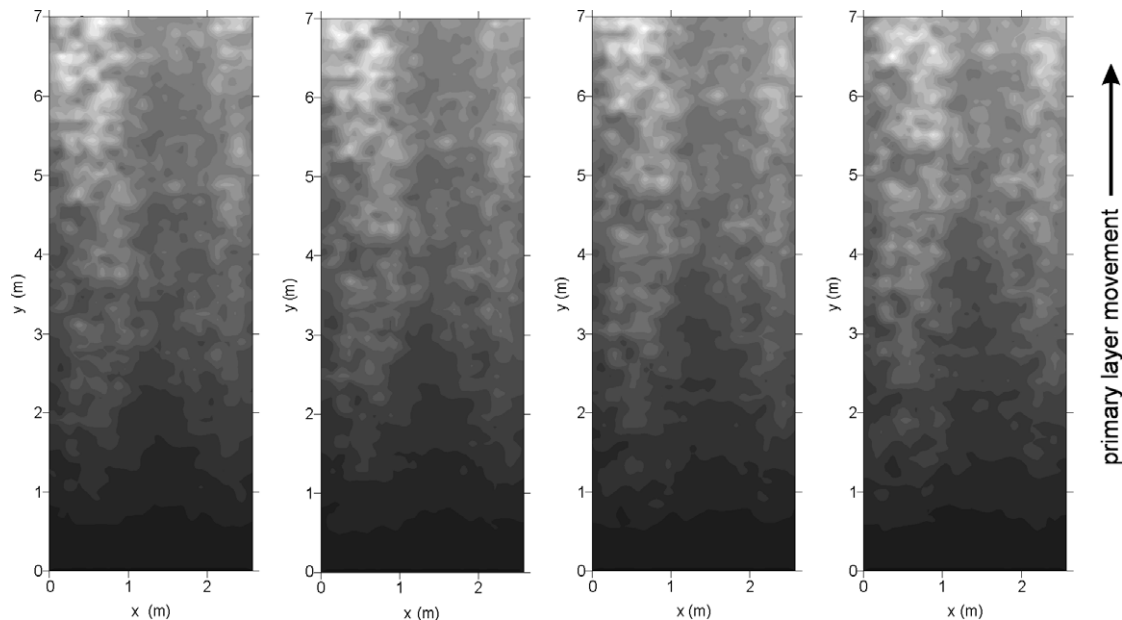

Fig. 8. Experimentally modelled successive images of the primary layer inside the collection chamber.

The momentum conservation equation is

$$\frac{\partial(\rho \bar{v}_i)}{\partial t} + \frac{\partial(\rho \bar{v}_j \bar{v}_j)}{\partial x_j}$$

$$= -\frac{\partial \bar{p}}{\partial x_i} + \frac{\partial}{\partial x_j}\left[\mu\left(\frac{\partial \bar{v}_j}{\partial x_j} + \frac{\partial \bar{v}_j}{\partial x_i}\right) - \rho\overline{v_i' v_j'}\right] + S_M. \quad (5)$$

The Reynolds stress tensor can be expressed with the Boussinesq approximation [10]. The closure of the set of the equations is simplified to the determination of the turbulent viscosity, which is usually determined by introduction of differential equations of the turbulence model. For the present case a two-equation k–ε RNG turbulence model by Launder and Spalding [11] was applied. Additional equations read

$$\frac{\partial(\rho k)}{\partial t} + \frac{\partial(\rho k \bar{v}_j)}{\partial x_j} = \frac{\partial}{\partial x_j}\left[\alpha_k \mu_{\text{eff}} \frac{\partial k}{\partial x_j}\right] + P_k - \rho\varepsilon \quad (6)$$

and

$$\frac{\partial(\rho\varepsilon)}{\partial t} + \frac{\partial(\rho\varepsilon \bar{v}_j)}{\partial x_j} = \frac{\partial}{\partial x_j}\left[\alpha_\varepsilon \mu_{\text{eff}} \frac{\partial\varepsilon}{\partial x_j}\right] + C_{1\varepsilon}\frac{\varepsilon}{k}P_k - C_{2\varepsilon}^*\rho\frac{\varepsilon^2}{k}, \quad (7)$$

where k is the turbulent kinetic energy, ε is the turbulent kinetic energy dissipation rate, α_k and α_ε are the inverse effective turbulent Prandtl numbers, μ_{eff} is the effective viscosity, P_k represents the generation of turbulent kinetic energy due to the mean velocity gradients and $C_{1\varepsilon}$ and $C_{2\varepsilon}^*$ are model coefficients.

Porous media are modelled by the addition of a momentum source term S_M to the standard fluid flow equations. The source term is composed of two parts, a viscous loss term and an inertial loss term. The source term reads as follows:

$$S_M = -\left(\sum_{i=1}^{3} D_{ij}\mu v_j + \sum_{i=1}^{3}\frac{1}{2}C_{ij}\rho|v_j|v_j\right), \quad (8)$$

where S_M is the source term for the ith (x, y, or z) momentum equation, and D and C are prescribed matrices of viscous and internal resistance, respectively. This momentum sink contributes to the pressure gradient in the porous cell, creating a pressure drop that is proportional to the fluid velocity (or velocity squared) in the cell.

3.1. Experimental determination of the space and time dependant porosity profile

The results of the visualization of the primary layer (Fig. 6) were used as the base for the input of the resistance distribution in the porous zone. Since the flow inside the primary layer is laminar, only the part of the momentum source term S_M (Eq. (8)) that is linearly dependent of the velocity (term D_{ij}) was used ($C_{ij} = 0$).

The thickness of the primary layer is relatively thin (maximum values (at point B in Fig. 1) range up to 10 mm), hence the hypothesis that the values of the gray level matrix (A_{ij}) and the values of the matrix of viscous resistance (D_{ij}) are linearly dependent, is valid. The matrix D_{ij} can be written as

$$D_{ij} = k \cdot A_{ij}. \quad (9)$$

The value of k was determined so that the predicted pressure drop at the transition trough the porous zone was the same as measured experimentally.

4. Simulation

The computational domain included the blower with the spinning wheels, the space behind the blower the wool chamber with the perforated mesh and the suction duct (Fig. 9).

When the grid of the computational domain was fine enough, almost no influence of the grid size was found. To study the grid influence the average velocity on a plane 50 mm upstream of the perforated mesh was monitored. The discretization error of 0.5% was estimated. Eventually a structured mesh with about 250 000 nodes was used. Standard wall functions were applied, hence the $y+$ value lies between 20 and 180.

The convergence criterion was determined by observing the evolution of different flow parameters (velocity magnitude at outlet, static pressure in a point behind the perforated mesh) in the computational domain. The monitored flow parameters were always converged after the sum of the imbalance of the transport equations between iterations over all cells in the computational domain (residuals of the variables: pressure, velocity, turbulent kinetic energy and dissipation of turbulent kinetic energy) fell below 10^{-3} (after the error residuals drop by 3 orders of magnitude). After that, a number of different values (10^{-3}, 10^{-4} and 10^{-5}) for residuals were tested (Table 1), but no significant difference in the solution was found. Eventually a criterion for the converged solution was set to the point when the residuals fell below 10^{-4}. Approximately 450 iterations were needed to obtain a converged solution. The iteration error of · 0.04% was estimated.
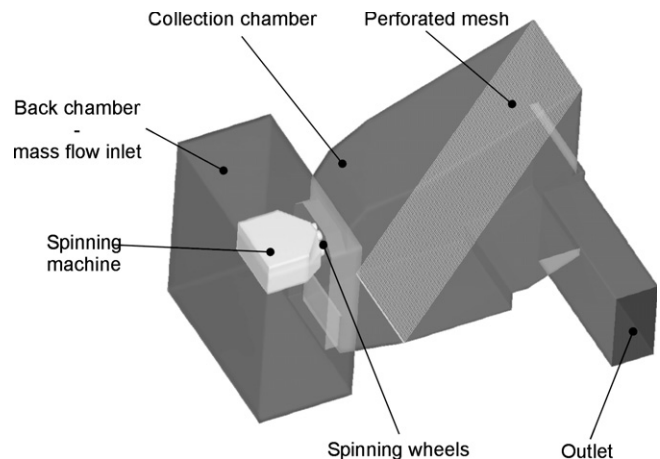

Fig. 9. Computational domain.

Table 1
Averaged calculated velocity $\bar{v}$ at different mesh sizes and residual values

Mesh size (–)	Residuals (–)	$\bar{v}$ (m/s)
≈250 000	<10^{-3}	6.829
≈250 000	<10^{-4}	6.847
≈250 000	<10^{-5}	6.848
≈125 000	<10^{-4}	6.812
≈1 000 000	<10^{-4}	6.851

Conditions applied for the simulation were the following:

– Velocity inlet: Imposed velocity at inlet nozzles: 100 m/s.
– Mass flow into the back chamber behind the blower: 45.3 kg/s.
– Pressure outlet: Imposed static pressure at the exit from the suction duct: 1 bar.

The values $\rho = 1.225$ kg/m^3 and $\mu = 1.789 * 10^{-5}$ Pa s for air density and dynamical viscosity were used for the simulation.

5. Results and discussion

The goal of the simulation was to test the hypothesis that the forming of the primary layer is significantly dependent on local aerodynamic characteristic of the airflow in the collection chamber.

Fig. 10 shows the predicted pathlines of the flow from the nozzles trough the primary layer, perforated mesh and into the exhaust.

One can see that the air flows through the perforated mesh predominately in the middle section. Because of the inclination of the perforated mesh it deviates upward just in front of it.

Fig. 11 shows the velocity distribution on a plane positioned 50 mm in front of the perforated mesh. The images correspond to the boundary conditions (primary layer distributions) shown in Fig. 8.
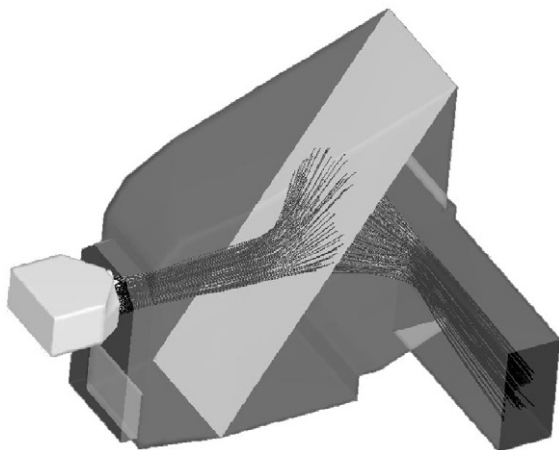

Fig. 10. Numerically predicted flow pathlines in the mineral wool chamber.

The core of the flow is in the middle section (as already seen from pathlines in Fig. 10) where higher velocities are predicted. It can be seen by comparison of mineral wool distributions and the velocity magnitude distributions that velocities are lower in the regions where the primary layer is thicker (where grey levels in Fig. 11 are lower (darker regions)). This relation applies that the velocity field and the primary layer distribution are interdependent – the primary layer thickness is small in the regions where the flow velocity is high.

Of interest is also the qualitative comparison of velocity distribution in Fig. 11, where a local velocity peak is significant in the region, where the blow-away airflow passes through the perforated mesh and the mineral wool primary layer. Due to local velocities, which can reach values up to 4 m/s [5] in the velocity peak region, the shredding of individual flocks from the already formed primary layer takes place. Those mineral wool flocks are then carried by the airflow in the direction of present velocity gradients and settle onto the forming primary layer in the regions of lower velocities. As a consequence, a non-homogeneous thickness of the primary layer due to rearrangement of the latter is expected. This assumption can be confirmed by the lateral (transverse) distribution of the mineral wool layer (Fig. 4), where the thickness of the primary layer is lower in the middle region and bounded by two thickness peaks on left and right side of the primary layer lateral cross-section.

It can also be concluded that the process has a self-homogenisation nature, as the flow tends to deviate from the regions where the primary layer is thicker to the regions with thinner primary layer. Higher flow rate in the region with thinner primary layer carries more molten rock fibre and therefore contributes to higher rate of accumulation of the primary layer in this region. After the primary layer thickness in the particular region grows the flow will deviate to the region with thinner region and accumulate more fibre there.

The histograms in Figs. 12–14 represent the distributions of velocity fluctuations (local standard deviation of velocity magnitude $\sigma(v)$) on sections 50 mm in front of the perforated mesh.

The qualitative similarity between histograms of velocity fluctuations in Figs. 12–14 and appropriate histograms of primary layer structure in Figs. 5–7 at specified transverse locations x can be observed. This conclusion implies that the quality of the primary layer of the mineral wool and velocity fluctuations inside the collecting chamber are closely related. The similarity between histograms complements the already researched similarities between velocity distributions of the flow on the perforated mesh and thickness distributions of the primary layer. These similarities indicate the interdependence between the flow properties – in the region where the flow passes through the primary layer – and the texture of the forming primary layer inside the collection chamber.
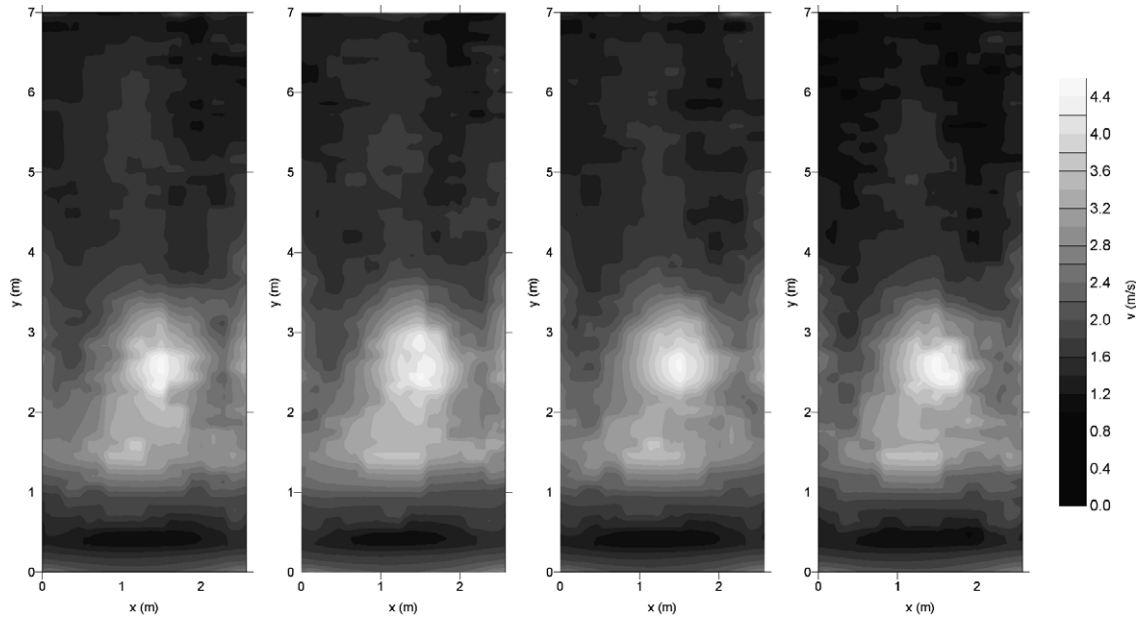
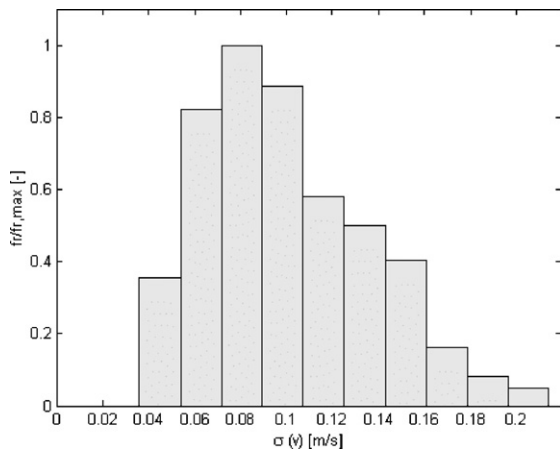Fig. 11. Time-dependent normal velocity component on the perforated mesh.

Fig. 12. Distribution of velocity fluctuations at $x = 53.5$ mm.
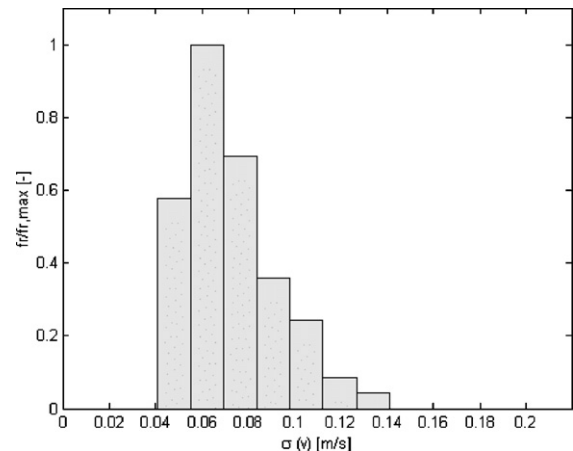

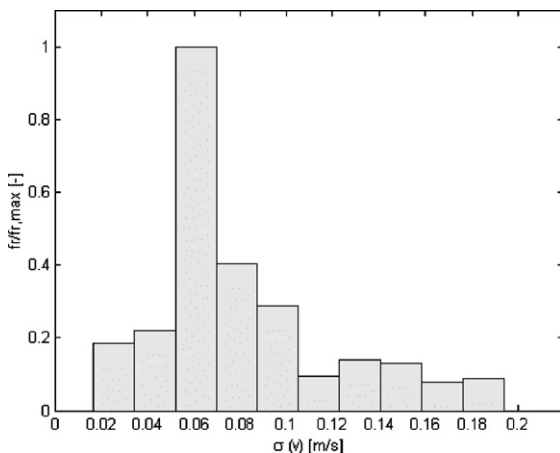Fig. 14. Distribution of velocity fluctuations at $x = 2519.5$ mm.

Fig. 13. Distribution of velocity fluctuations at $x = 1286.5$ mm.

6. Conclusions

The paper presents a research of the airflow aerodynamic characteristics in a chamber where mineral wool is produced. It is mainly focused on a study of basic mechanisms of mineral wool primary layer formation in the blow-away airflow from the spinning machine to the region of perforated mesh inside the collection chamber. The process of primary layer formation on a moving perforated mesh is described and the problems of non-uniform wool fibres distribution are analysed.

In order to determine the correlation between the structure of the mineral wool primary layer and the velocity field, two different methods were applied. The experimental method of computer-aided visualization enabled evaluation of a mineral wool texture inside the primary layer. On the other hand, a numerical model was developed,

which incorporated real time-dependent boundary conditions to predict the velocity field inside the collection chamber, since the experimental verification of flow conditions in the real process of primary layer formation was not possible. Gained results showed significant influences of local turbulent properties of the airflow on the primary layer formation, which lead to the following main conclusions:

– Texture of the primary layer is subordinated to the $-5/3$ cascade law of the eddy structure decay in the airflow in the region of primary layer formation.
– Velocity field inside the collection chamber shows significant velocity peak, which is the consequence of the axial blow-away airflow from the spinning machine nozzles. This phenomenon causes shredding of the already formed primary layer and fibre rearrangement, which is also confirmed by the time averaged mean transverse distribution of mineral wool in the primary layer at the outlet of the collecting chamber.

The stated conclusions are supported by the similarities between histograms of the velocity fluctuation distribution and those of the structural fluctuation distribution in the texture of the primary layer.

The paper addresses the variables, which significantly influence the homogeneity of fibre distribution inside the collection chamber. Negative influence of local velocity anomalies is emphasized on large scales as well as on small ones. It can be concluded that the more homogeneous primary layer can be expected when the values of local velocity peaks are decreased, which is in turn connected with the blow-away on the spinning machine. Apart from that, the homogeneous and isotropic turbulent conditions inside the collection chamber could lead to a finer and more homogeneous texture of the primary layer, which is one of the aims of the mineral wool production process.

References

[1] I. Ohberg, Technological development of the mineral wool industry in Europe, Annals of Occupational Hygiene 31 (4B) (1987) 529–545.
[2] F. Trdič, B. Širok, P.R. Bullen, D.R. Philpott, Monitoring mineral wool production using real-time machine vision, Real Time Imaging 5 (2) (1999) 125–140.
[3] A.W. Angwafo, P.R. Bullen, D.R. Philpott, Melt flow in the production of mineral wool by centrifugal spinning, in: Proc. FEDSM'98 ASME Fluids Eng. Div. Summer Meeting, Washington, USA, June 21–25, 1998.
[4] T. Westerlund, T. Hoikka, On the modeling of mineral fiber formation, Computers and Chemical Engineering 13 (10) (1989) 1153–1163.
[5] B. Širok, B. Blagojević, M. Novak, Influence of blow away velocity field on the primary layer fibre structure in the mineral wool production process, Glass Technology 43 (5) (2002) 188–194.
[6] B. Blagojević, B. Širok, Multiple regression model of mineral wool fibre thickness on a double-disc spinning machine, Glass Technology 43 (3) (2002) 120–124.
[7] B. Blagojević, B. Širok, M. Hočevar, Monitoring and control of quality of the primary layer of on a disc spinning machine, Instrumentation Science and Technology 31 (1) (2003) 63–75.
[8] W.D. McComb, The Physics of Fluid Turbulence, Oxford University Press, Oxford, 1996.
[9] S.V. Patankar, Numerical Heat and Fluid Flow, Hemisphere, New York, 1980.
[10] J.L. Ferziger, M. Perić, Computational Methods for Fluid Dynamics, Springer-Verlag, Heidelberg, 2002.
[11] B.E. Launder, D.B. Spalding, The numerical computation of turbulent flows, Computer Methods in Applied Mechanics and Engineering 3 (1974) 269–289.